How stress triaxiality affects cavitation damage in high-density polyethylene: Experiments and constitutive modeling

Amar Mesbah [a], Mohamed Elmeguenni [b], Zhu Yan [b], Fahmi Zaïri [b,*], Ning Ding [c,*], Jean-Michel Gloaguen [d]

[a] University of Sciences and Technology Houari Boumediene, Laboratory of Advanced Mechanics, 16111, Algiers, Algeria
[b] University of Lille, Civil Engineering and geo-Environmental Laboratory (ULR 4515 LGCgE), 59000, Lille, France
[c] Qilu University of Technology (Shandong Academy of Sciences), Engineering Research Center of Failure Analysis and Safety Assessment, Shandong Analysis and Test Center, 250014, Jinan, China
[d] University of Lille, Unité Matériaux et Transformations (UMR CNRS 8207 UMET), 59000, Lille, France

A B S T R A C T

The aim of this article is to investigate how the stress triaxiality affects the plastic deformation behavior of high-density polyethylene using an approach combining experiments and micromechanics-based modeling. The stress-strain behavior along with the cavitation damage accumulation are experimentally quantified under well-controlled transversal response of hourglass-shaped tensile specimens with different curvature radii in order to set different triaxial stress states in the median cross-section. A constitutive elastic-plastic-damage representation is then presented within a continuum-based micromechanical framework. The model, constrained by the same boundary conditions as the experimental tests, is used to examine the stress triaxiality effects on the separate and synergistic effects of plasticity and cavitation damage micromechanisms that govern the macro-response.

1. Introduction

Semi-crystalline polyethylene is widely used in engineering components in most fields of technology (oil industry, automobile, aeronautic, robotic, biomechanics, civil engineering, etc.) and may experience more or less complex mechanical loadings. The assessment of their intrinsic mechanical behavior is of prime importance in the design of polyethylene components whether in the form of fibres, films or massive parts. From this standpoint, the establishment of the structure-property relationship is particularly important [1–7]. From the earlier studies of Peterlin [8,9] the prevailing picture for plastic deformation in straining of a semi-crystalline polymer has been stated as the destruction of lamellae associated with their unraveling and transformation into densely packed microfibrils, all thought to occur in a catastrophic process termed micronecking. Over the years, a substantial qualitative understanding of the plasticity/damage interactions has been brought [10–16]. The applied tensile stress causes in the first place the deformation of polymer amorphous phase. In polyethylene its modulus is low, so its deformation is rather high. Under such strain the amorphous phase loses its consistency and cavitation can occur. That is also connected

with 3D stress being developed in thin amorphous layers embedded between broad and wide lamellae. Amorphous layers have limited possibilities to expand or shrink in the directions along the contact with crystalline lamellae, so cavitation occurs. In many polymers, including polyethylene, the cavitation of the amorphous phase can be the first plastic deformation event and then the tensile yielding is in fact determined by the strength and consistency of the amorphous phase and not by crystal plasticity. The stress triaxiality may affect the plasticity/-damage coupling. It is the case, for example, during the appearance of a necking or in a crack tip where triaxiality effects and plasticity/damage coupling are combined [17–19]. The triaxiality effects on the constitutive behavior can be studied by loading in tension cylindrical hourglass-shaped specimens with different curvature radii [20–23]. The simultaneous investigation of the triaxiality effects and the plasticity/-damage coupling remains rarely documented.

Over the years, constitutive representations of the polyethylene have been proposed. Although purely phenomenological approaches can be employed [24–27], continuum-based constitutive models considering structural parameters may provide a deeper understanding of the intrinsic mechanical behavior and a more accurate information in the

---

design of polyethylene components. According to the approximation of the microstructure based on composite-type representations, the macro-response may be modeled by the averaging homogenization performed within a mesoscopic representative volume element. By this way, the active interactions of the amorphous and crystalline domains are modeled. For example, research works [20,28–30] proposed models based on the Eshelby inclusion theory and the micromechanics framework using the matrix-inclusion constitutive representation to predict elastic stiffness and yield strength of semicrystalline polymer systems. As an alternative, the semicrystalline structure may be regarded as an aggregate of two-phase inelastic layered composite inclusions to predict both pre-yielding and post-yielding [31–38]. Treating also such material systems as two-phase media, rheological inelastic constitutive models were also proposed [39–50]. If the aforementioned models are able to bring a better understanding of the crystallization on the macro-response, their application is relevant only if the deformation results exclusively from isochoric deformation mechanisms, which excludes the inelastic dilatation mechanisms.

The aim of the present article is to investigate how the stress triaxiality influences the stress-strain behavior along with the cavitation damage in high-density polyethylene. We report experimental observations carried out under well-controlled transversal response of hourglass-shaped tensile specimens with different curvature radii in order to set different triaxial stress states in the median cross-section. A constitutive elastic-plastic-damage representation of high-density polyethylene is then presented within a continuum-based micromechanical framework in order to provide a deeper understanding of the separate and synergic effects of plasticity and cavitation damage micromechanisms on the macro-response.

The present paper is organized as follows. The investigated material, experimental procedures and results are detailed in Section 2. Section 3 presents the continuum-based micromechanical model, a parametric study and the model-experiments comparisons. Concluding remarks are finally given in Section 4.

2. Experiments

2.1. Material and methods

2.1.1. Material and specimens

The investigated high-density polyethylene is a grade used for pipe applications. Cylindrical hourglass-shaped tensile specimens were extracted from the same pipe, parallelly to the extrusion direction. The specimen geometry, with curvature radii R_{c0} equal to 2, 4, 10 and 80 mm, is given in Fig. 1a. They will be referred to as Rx where x is the initial curvature radius value. The initial specimen dimension is defined by the curvature radius R_{c0}, the minimum diameter D_0, the gage length L_0, and the maximum diameter W. The gage length L_0 is equal to 4, 7, 13 and 40 mm for R2, R4, R10 and R80, respectively. All specimens have the same D_0 and W values.

The main characteristics provided by the manufacturer (STPM CHIALI Company) are: density $\approx$ 0.96 g/cm^3, weight-average molar weight $\approx$ 310,000 g/mol and carbon black $\approx$ 2.5%. The crystallinity ratio was determined by means of a PerkinElmer Diamond differential scanning calorimetry (DSC) at a heating rate of 10 °C/min under nitrogen atmosphere. It was verified that all DSC measurements are the same on the second run. Measurements were taken on specimens of 10 mg cut in three positions of the pipe thickness (Fig. 1b); the outer and inner diameters are of 250 mm and 232 mm, respectively. Using a theoretical melting enthalpy of the pure crystalline polyethylene material of 289 J/g [51], a crystallinity ratio of approximately $\varphi_w^{cry} = 74\%$ was found for the three positions.

2.1.2. Mechanical testing

The tension tests were achieved in well-controlled conditions, at room temperature and at constant true strain rate, up to failure by means of a video-controlled system in order to determine the intrinsic tension behavior of the high-density polyethylene material. The tests were performed using an electromechanical Instron-5800 universal testing machine equipped with suitable testing rigs. As shown in Fig. 2 a CCD camera, connected with the testing machine, records the minimum diameter of the specimen. In order to investigate how the stress triaxiality affects the nonlinear material response in relation with the deformation mechanisms, two different measurements have been undertaken in the plastic instability:

- **Tests with a constant cross-head speed up to failure:** The video-system is used as a simple extensometer in order to record the decrease of the minimum diameter while the cross-head speed of the Instron testing machine is constant.
- **Tests with a constant local true strain rate up to failure:** The device enables us to impose (locally in the smallest section of the necking) a constant rate of the true diametral strain $\bar{\varepsilon}_D = \ln D/D_0$ by regulating the cross-head speed of the Instron testing machine.

By designating the 1-direction as axisymmetric axis of the cylindrical hourglass-shaped tensile specimen and the transverse plane 2–3 to be the cross-section, the effective stress $\bar{\sigma}$ can be written as[1]:

$$\bar{\sigma} = \mathrm{diag}\left(\bar{\sigma}_{11}, R\bar{\sigma}_{11}, R\bar{\sigma}_{11}\right) \tag{1}$$

in which $R = \bar{\sigma}_{22}/\bar{\sigma}_{11} = \bar{\sigma}_{33}/\bar{\sigma}_{11}$ is the stress ratio.

The mean stress $\bar{\sigma}_m$ and the von Mises equivalent stress $\bar{\sigma}_{eq}$ are expressed as:

$$\bar{\sigma}_m = \frac{\bar{\sigma}_{11}}{3}(1 + 2R) \tag{2}$$

$$\bar{\sigma}_{eq} = \bar{\sigma}_{11}(1 - R) \tag{3}$$

The two limit values $R = 0$ and $R = 1$ correspond, respectively, to the uniaxial tension case and the pure hydrostatic case. The multiaxial stress state in the median cross-section of the specimen can be quantified using the stress triaxiality ratio β, a scalar quantity defined as the ratio of the mean stress $\bar{\sigma}_m$ and the von Mises equivalent stress $\bar{\sigma}_{eq}$:

$$\beta = \frac{\bar{\sigma}_m}{\bar{\sigma}_{eq}} = \frac{1 + 2R}{3(1 - R)} \tag{4}$$

The initial maximum stress triaxiality β, reached at the center of the median cross-section, is given in Fig. 1b for each studied specimen by using a Bridgman [52] analysis. As expected, it increases with decreasing curvature radius R_{c0}, from 0.33 for R80 specimen to 0.8 for R2 specimen.

2.1.3. Volumetric strain measurements

The 2D images during deformation were monitored and treated with an image analysis software in order to calculate the current volume V after 3D reconstruction of the specimen gage part. Solely the latter is assumed to be concerned by the volume variation. Straight cross-sections are supposed to remain straight during deformation. An example of obtained result after 3D reconstruction is shown in Fig. 2 for different load sequences of a R2 specimen.

The true volumetric strain $\bar{\varepsilon}_V$ is given by:

$$\bar{\varepsilon}_V = \ln\left(\frac{V}{V_0}\right) \tag{5}$$

where V_0 is the initial volume the specimen gage part.

---

[1] Tensors are denoted by normal boldfaced letters while scalars and individual components of tensors are denoted by normal italicized letters.
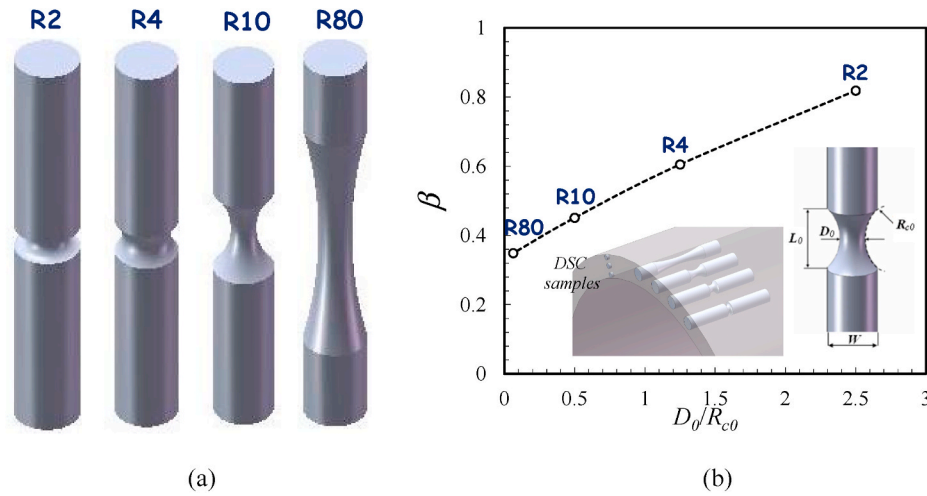
Fig. 1. Hourglass-shaped tensile specimens: (a) geometry with four different curvature radii R_{c0} (For all specimens, the initial minimum diameter D_0 is equal to 5 mm and the maximum diameter W is equal to 10 mm), (b) initial maximum stress triaxiality β for each specimen.
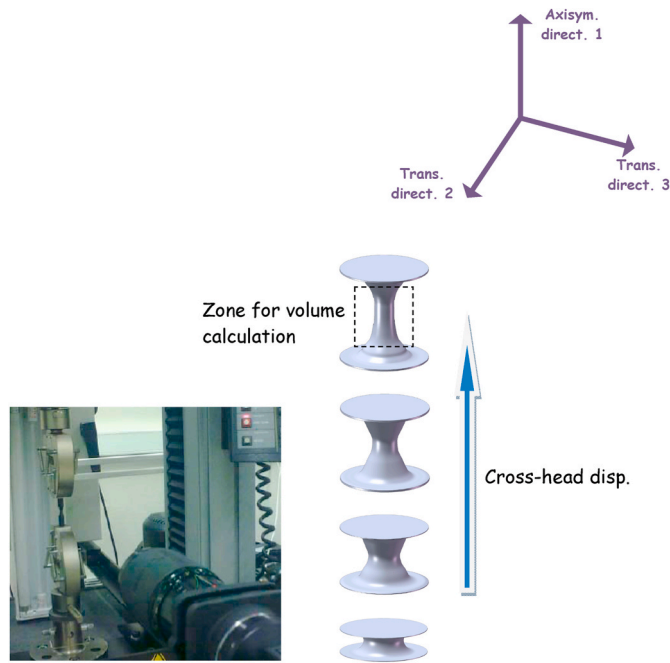

Fig. 2. Experimental device for the measurements of the smallest cross-section of the hourglass-shaped tensile specimens. After 3D reconstruction from the recorded 2D images, the volumetric strain is calculated in the specimen gauge zone.

The true inelastic volumetric strain $\overline{\varepsilon}_{Vcav}$ is determined by eliminating the Poisson's ratio contribution by substituting the elastic part $\overline{\varepsilon}_{Vel}$:

$$\overline{\varepsilon}_{Vcav} = \overline{\varepsilon}_V - \overline{\varepsilon}_{Vel}, \ \overline{\varepsilon}_{Vel} = (1-2\nu)\frac{\overline{\sigma}_{11}}{E} \tag{6}$$

in which ν is the elastic Poisson's ratio, E is the Young's modulus, $\overline{\sigma}_{11} = 4F/\pi D^2$ is the true axial stress, F is the actual value of the applied load and D is the minimum diameter of the deformed specimen.

This inelastic volumetric strain allows differentiating the dilatational

mechanisms, giving rise to a volume increase, and the shear yielding, occurring at constant volume [53,54]:

$$\overline{\varepsilon}_{shear} = \overline{\varepsilon}_{11} - \overline{\varepsilon}_{Vcav} - \overline{\varepsilon}_{Vel} \tag{7}$$

where $\overline{\varepsilon}_{11}$ is the true axial strain.

2.2. Experimental results

2.2.1. Transversal behavior

The results of tensile tests achieved at constant cross-head speed on the four hourglass-shaped specimens are firstly analyzed. The diametral strain measured during the tensile test at constant cross-head speed can be considered as a cavitation damage indicator [21]. Fig. 3a shows the evolution of the true diametral strain against the true axial strain (defined as the natural logarithm of the ratio of the gage length to the initial gage length), and the consequences of triaxialities higher than that of a uniaxial loading. All tests were performed at a nominal strain rate (defined as ratio of the constant cross-head speed and the gage length) of 0.001 s^{-1}. Recall that the initial minimal diameter is the same for all the specimens. It can be clearly observed that the lower the curvature radius (i.e. the higher the stress triaxiality) is, the lower the diameter reduction is. The cavitation phenomenon is expected to be more pronounced for the higher triaxialities. The diameter reduction for the lowest triaxiality tends to an asymptotic value, this stabilization corresponding to the neck propagation stage.

The results of tensile tests carried out by controlling the diameter reduction are now examined. To this end, the cross-head speed is regulated during the test. The variation of the true axial strain with time is given in Fig. 3b. It can be seen that the diametral strain progresses linearly with time whereas the axial strain exhibits different stages which can be correlated with the different steps of the stress-strain response.

2.2.2. Stress-strain responses

The true stress-strain curves and the evolution of the deformation mechanisms for the four hourglass-shaped tensile specimens stretched at a constant local true strain rate of 0.001 s^{-1} are presented in Fig. 4. The specimens always behave in a very ductile manner. The actual shape of specimens, obtained from the CCD camera at different levels of strain, is also presented in the figure. All specimens exhibit a symmetric
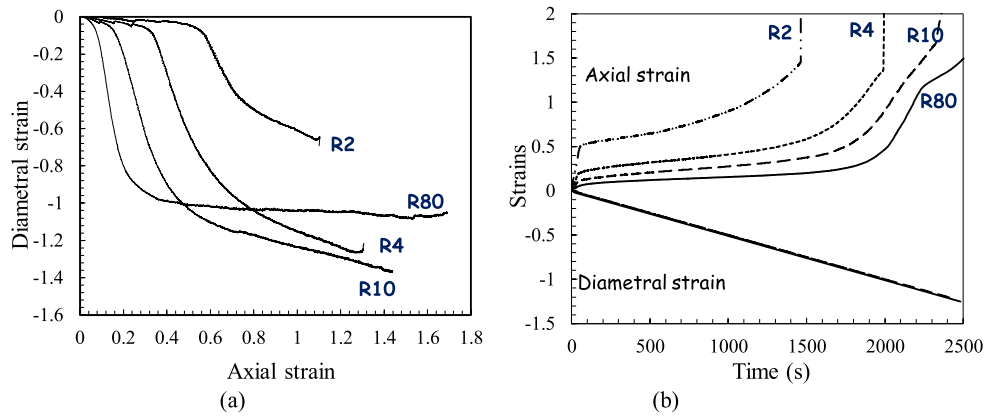
Fig. 3. Strain evolutions under tensile tests at (a) constant cross-head speed and (b) constant local true strain rate.
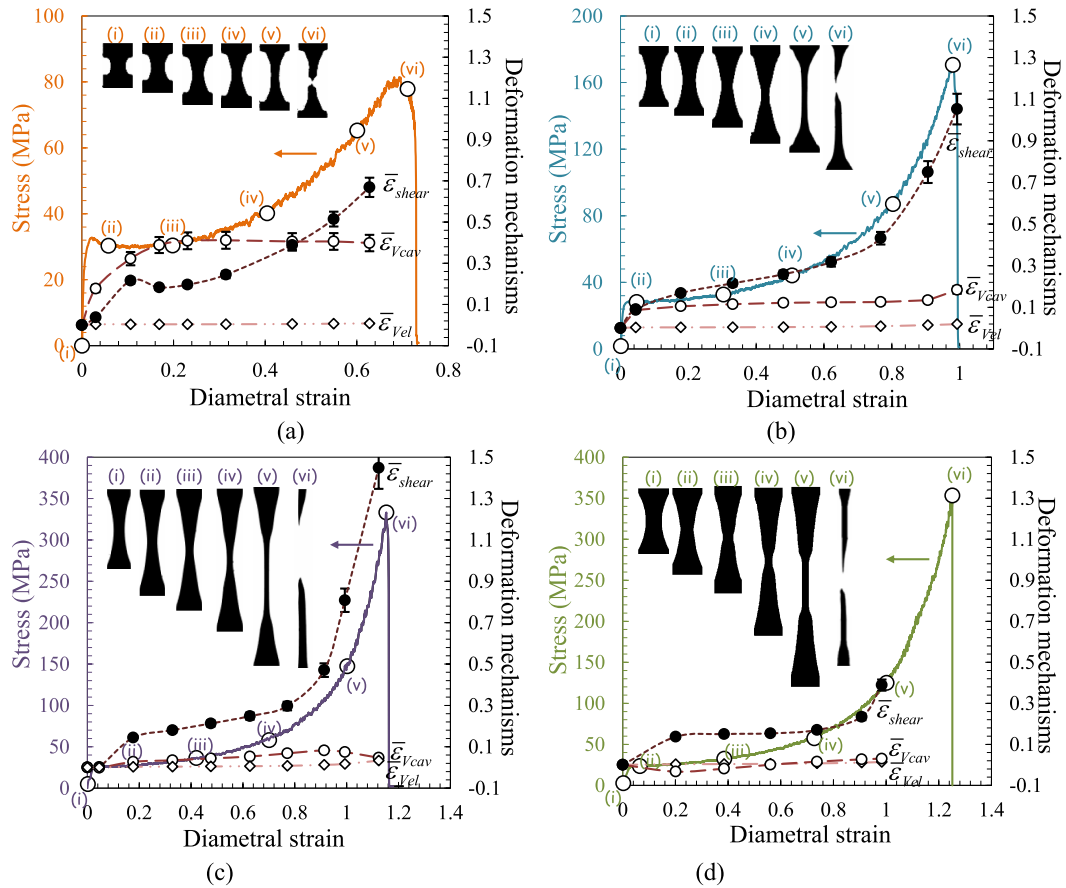

Fig. 4. Stress-strain curves and deformation mechanisms in high-density polyethylene for (a) R2, (b) R4, (c) R10 and (d) R80 specimens. The specimen shape evolution in the course of tension is given for different strain levels from the initial state to the final failure state. The quantities $\overline{\varepsilon}_{shear}$, $\overline{\varepsilon}_{Vcav}$ and $\overline{\varepsilon}_{Vel}$ denote, respectively, the shearing strain, the cavitation damage strain and the elastic strain.

propagation of the necking initiated at the median cross-section. The curvature radius becomes larger while the necking continues to increase and at very large strains the specimens look like smooth specimens. The stress-strain behavior is characterized by four main stages: an initial elastic response, followed by a rollover to yield, a progressive plastic strain hardening and finally a dramatic plastic strain hardening at very large strains before final rupture. Some strain softening is observed just

after yielding for the highest triaxiality that would be the consequence of an exacerbated damage. By comparing the different stress-strain curves, it can be observed that the stress triaxiality has an important effect on the strain hardening. It can be also observed that the higher the stress triaxiality is, the lower the diametral strain at failure is. The ultimate diametral strain is decreased by about 50% for stress triaxialities varying between 0.33 and 0.8.

2.2.3. Deformation mechanisms

According to the earlier studies of Peterlin [8,9] the shear yielding is identified as the mechanisms operating in the crystalline lamellae; the plasticity of the crystalline lamellae is followed by their fragmentation leading to the formation of a fibrillar microstructure. The inelastic volumetric strain is the most direct indicator of the voiding mechanism nucleated within the amorphous phase between the crystalline lamellae. The components of the deformation mechanisms, determined at different levels of plastic strain, are reported in Fig. 4. According to the stress triaxiality ratio, a competition between two inelastic mechanisms is clearly pointed out: plasticity/fragmentation mechanisms of crystalline lamellas vs. voiding mechanism. It appears that the shear yielding is the predominant deformation mechanism for the lowest triaxialities. By contrast, for the highest triaxiality, in which high hydrostatic stresses are involved, the inelastic volumetric strain takes over the shear strain and takes place as the plastic deformation proceeds. For all the triaxialities the rate of volumetric strain decreases at very large strains. It appears that two competing mechanisms control the macroscopic rupture of the high-density polyethylene material: destruction of the lamellar morphology and stretching limit of the chains at low triaxiality and, coalescence process of microvoids at high triaxiality.

To confirm the observations made at the macroscopic scale, the breaking surfaces of hourglass-shaped specimens were examined at various scales using a Hitachi S 4700 scanning electron microscope operated at an accelerating voltage of 10 kV. The surfaces were observed perpendicularly to the direction of applied stress. The morphological characteristics of specimens presenting the two extreme triaxialities are presented in Fig. 5. In the case of a low triaxiality one can note the presence of some voids which do not seem to interact with each other. At high triaxiality, the situation is completely different and the observations confirm the preponderant character of the damage by void growth.

3. Micromechanics-based elastic-plastic-damage model

3.1. Constitutive equations

In order to bring a better understanding of the triaxiality effects on the elastic-plastic response along with the cavitation damage in high-density polyethylene, a constitutive model based upon the continuum-based micromechanical framework is presented in this section. The morphological representation of the said material is treated as an Eshelby-type inclusion problem in which the representative volume element consists in a stiff percolated crystalline medium as the continuous phase and a discrete rubbery amorphous phase with an original volume fraction φ_0^{am}. This morphological representation was initially proposed by Hachour et al. [20] to capture the initial biaxial yield strength and is extended here to the plastic-damage behavior. Since our objective is to model the overall yielding behavior, rather than the elementary mechanisms operating in the crystalline lamellae, the ensemble-volume averaged homogenization procedure can be directly used, the active interaction between crystalline and amorphous domains being considered as a first-order factor. The two constitutive phases are supposed to be isotropic and homogeneous media with elastic stiffness tensors $\mathbf{C}^{cry}$ and $\mathbf{C}^{am}$. The stiff crystalline matrix behaves in a purely deviatoric manner (without volume change) and is described by the von Mises yield criterion with isotropic plastic hardening.

The elastic constitutive relation is given by[2]:

$$\overline{\boldsymbol{\sigma}} = \overline{\mathbf{C}} : \overline{\boldsymbol{\varepsilon}}^e \tag{8}$$

in which $\overline{\boldsymbol{\sigma}}$ is the effective stress given in Eq. (1) in axisymmetric form, $\overline{\mathbf{C}}$

is the effective elastic stiffness and $\overline{\boldsymbol{\varepsilon}}^e$ is the effective elastic strain expressed as:

$$\overline{\boldsymbol{\varepsilon}}^e = \text{diag}\left(\varepsilon_{11}^e, \varepsilon_{22}^e, \varepsilon_{22}^e\right) = \frac{\overline{\sigma}_{11}}{E}\,\text{diag}(1 - 2\nu R, \, -\nu + (1-\nu)R, \, -\nu + (1-\nu)R) \tag{9}$$

where E and ν are again, respectively, the (effective) elastic stiffness and the (effective) Poisson's ratio of the semi-crystalline material.

The effective plastic strain rate $\dot{\overline{\boldsymbol{\varepsilon}}}^p$ is governed by the normality rule and corresponds to the differentiation of the effective yield function $\overline{F}$ with respect to the effective stress $\overline{\boldsymbol{\sigma}}$:

$$\dot{\overline{\boldsymbol{\varepsilon}}}^p = \dot{\lambda}\frac{\partial \overline{F}}{\partial \overline{\boldsymbol{\sigma}}} = (1 - \varphi^{am})\dot{\lambda}\frac{\overline{\mathbf{T}} : \overline{\boldsymbol{\sigma}}}{\sqrt{\overline{\boldsymbol{\sigma}} : \overline{\mathbf{T}} : \overline{\boldsymbol{\sigma}}}} \tag{10}$$

where $\dot{\lambda}$ is the plastic multiplier and φ^{am} is the current amorphous volume fraction:

$$\varphi^{am} = \varphi_0^{am} - \varphi^{cav} \tag{11}$$

in which the term φ^{cav} represents the cavitation damage.

The effective yield function $\overline{F}$ is dependent on the mean stress and is given by Ref. [55]:

$$\overline{F} = (1 - \varphi^{am})\sqrt{\overline{\boldsymbol{\sigma}} : \overline{\mathbf{T}} : \overline{\boldsymbol{\sigma}}} - \sqrt{\frac{2}{3}}\left[\sigma_y + \xi(\overline{e}^p)\right] \leq 0 \tag{12}$$

in which σ_y is the initial yield strength of the crystalline phase and $\xi(\overline{e}^p)$ is a function of the effective equivalent plastic strain $\overline{e}^p$:

$$\xi(\overline{e}^p) = h_1(\overline{e}^p)^{q_1} + h_2(\overline{e}^p)^{q_2} \tag{13}$$

in which the terms h_1, h_2, q_1 and q_2 are the hardening parameters of the crystalline phase.

It is worth noticing that the triaxiality-dependence is supposed entirely due to the amorphous phase. Indeed, the usual von Mises yield criterion is recovered when the amorphous volume fraction is zero.

The term $\overline{\mathbf{T}}$ is expressed as:

$$\overline{T}_{ijkl} = \overline{T}_1\delta_{ij}\delta_{kl} + \overline{T}_2\left(\delta_{ik}\delta_{jl} + \delta_{il}\delta_{jk}\right) \tag{14}$$

where δ_{ij} signifies the Kronecker delta, $\overline{T}_1$ and $\overline{T}_2$ are provided in Appendix A.

The terms $\overline{\mathbf{T}} : \overline{\boldsymbol{\sigma}}$ and $\overline{\boldsymbol{\sigma}} : \overline{\mathbf{T}} : \overline{\boldsymbol{\sigma}}$ write:

$$\overline{\mathbf{T}} : \overline{\boldsymbol{\sigma}} = \overline{\sigma}_{11}\text{diag}\left(\overline{T}_1 + 2R\overline{T}_1 + 2\overline{T}_2, \overline{T}_1 + 2R\overline{T}_1 + 2R\overline{T}_2, \overline{T}_1 + 2R\overline{T}_1 + 2R\overline{T}_2\right) \tag{15}$$

$$\overline{\boldsymbol{\sigma}} : \overline{\mathbf{T}} : \overline{\boldsymbol{\sigma}} = \overline{\sigma}_{11}^2\left[\overline{T}_1 + 2\overline{T}_2 + 4R\overline{T}_1 + 4R^2\left(\overline{T}_1 + \overline{T}_2\right)\right] = \overline{\sigma}_{11}^2\Phi(R) \tag{16}$$

The effective plastic strain rate $\dot{\overline{\boldsymbol{\varepsilon}}}^p$ becomes:

$$\dot{\overline{\boldsymbol{\varepsilon}}}^p = \frac{(1 - \varphi^{am})\dot{\lambda}}{\sqrt{\Phi(R)}}\text{diag}\left(\overline{T}_1 + 2R\overline{T}_1 + 2\overline{T}_2, \overline{T}_1 + 2R\overline{T}_1 + 2R\overline{T}_2, \overline{T}_1 + 2R\overline{T}_1 + 2R\overline{T}_2\right) \tag{17}$$

The effective elastic stiffness tensor $\overline{\mathbf{C}}$ is expressed as [56]:

$$\overline{\mathbf{C}} = \mathbf{C}^{cry}.\left\{\mathbf{I} - [\mathbf{Y}^{am} + \mathbf{Y}^{cav}].[\mathbf{S}^{am}.\mathbf{Y}^{am} + \mathbf{S}^{cav}.\mathbf{Y}^{cav} + \mathbf{I}]^{-1}\right\} \tag{18}$$

The terms $\mathbf{S}^{am}$ and $\mathbf{S}^{cav}$ denote the Eshelby tensors for the (intact) amorphous phase and the damaged amorphous phase, $\mathbf{I}$ is the identity tensor and, $\mathbf{Y}^{am}$ and $\mathbf{Y}^{cav}$ are tensors expressed as:

$$\mathbf{Y}^{am} = -\varphi^{am}\left[\mathbf{S}^{am} + (\mathbf{C}^{am} - \mathbf{C}^{cry})^{-1}.\mathbf{C}^{cry}\right]^{-1} \tag{19}$$

$$\mathbf{Y}^{cav} = -\varphi^{cav}(\mathbf{S}^{cav} - \mathbf{I})^{-1} \tag{20}$$

The cavitation damage is expressed by a two-parameter Weibull

---

[2] The double dot ":" signifies the tensor contraction between a fourth-order tensor and a second-order tensor, while the single dot "." denotes the tensor multiplication between two fourth-order tensors.
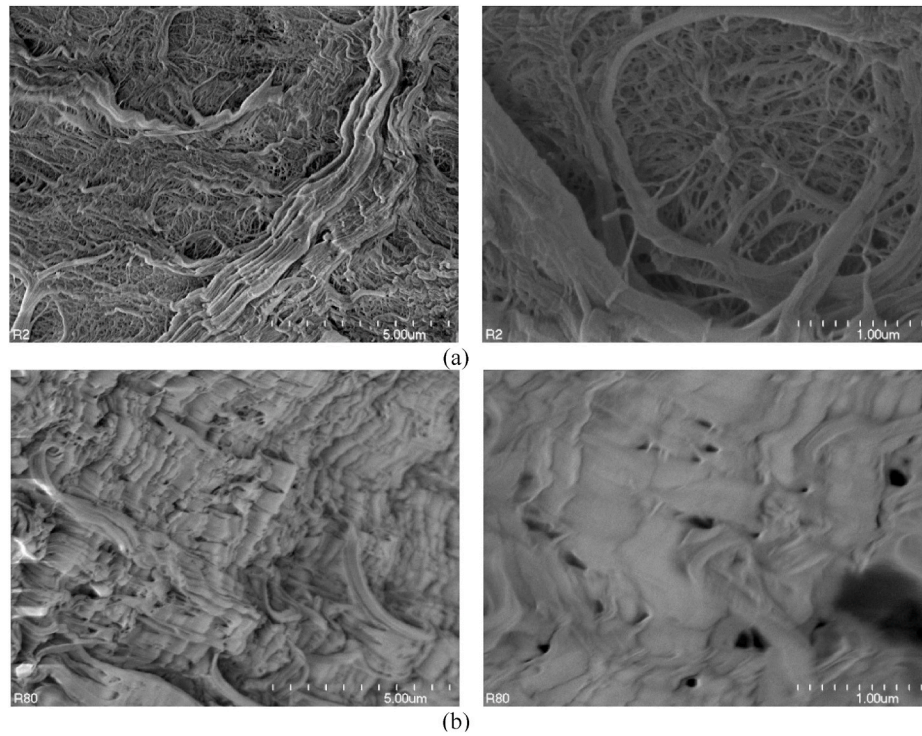
(a)

(b)

Fig. 5. SEM micrographs around the crack initiation site of (a) R2 specimen revealing voids and of (b) R80 specimen revealing non-interacting voids.

statistical distribution in order to introduce the stochastic nature of the process:

$$\varphi^{cav} = \varphi_0^{am}\left\{1 - \exp\left[-\left(\frac{\overline{\sigma}_m^{am}}{s}\right)\right]^m\right\} \tag{21}$$

in which m is the Weibull shape parameter, s is the Weibull scale parameter and $\overline{\sigma}_m^{am}$ is the mean of the internal stress $\overline{\boldsymbol{\sigma}}^{am}$ in the amorphous phase:

$$\begin{aligned}\overline{\boldsymbol{\sigma}}^{am} = \mathbf{C}^{cry}.\left\{\mathbf{I} + (\mathbf{I} - \mathbf{S}^{am}).\left[\mathbf{S}^{am} + (\mathbf{C}^{am} - \mathbf{C}^{cry})^{-1}.\mathbf{C}^{cry}\right]^{-1}\right\}.\\ \left\{\mathbf{I} + \mathbf{Y}^{am} + \mathbf{Y}^{cav} - [\mathbf{S}^{am}.\mathbf{Y}^{am} + \mathbf{S}^{cav}.\mathbf{Y}^{cav}]\right\}^{-1}.(\mathbf{C}^{cry})^{-1}:\overline{\boldsymbol{\sigma}}\end{aligned} \tag{22}$$

The model makes possible to estimate the separate and synergic effects of plasticity and cavitation damage. The model is now compared to the tension experimental data presented above. Note that in the literature the most reliable data on polymer crystal plasticity are collected in compression and in channel die compression, but not in tension. Nonetheless, it is obvious that the yielding due to tensile straining is not

connected with crystal plasticity but with the phenomena occurring in the amorphous phase.

3.2. Micromechanical simulation

Unless explicitly otherwise stated, the values of the model parameters are those listed in Table 1. The elastic stiffness of the amorphous phase E_{am} is given by:

$$E_{am} = 2(1 + \nu_{am})\frac{\rho_{am}R_u\theta}{M_{am}} \tag{23}$$

in which ν_{am} is the amorphous Poisson's ratio, $\rho_{am} = 0.855$ g/cm^3 is the density, $M_{am} = 1.4$ kg/mol is the molar mass between entanglements above the glass transition temperature, R_u is the universal gas constant and θ is the absolute temperature. The initial amorphous volume fraction φ_0^{am} is computed using the following relationship:

$$\varphi_0^{am} = 1 - \varphi^{cry} = 1 - \frac{\rho}{\rho_{cry}}\varphi_w^{cry} \tag{24}$$

Table 1
Model parameters.

| Parameter	Significance	Value
α	Shape factor	0.2
φ_0^{am}	Initial volume fraction	0.29
E_{am} (MPa)	Amorphous elastic stiffness	4.5
ν_{am}	Amorphous Poisson's ratio	0.49
E_{cry} (MPa)	Crystalline elastic stiffness	4500
ν_{cry}	Crystalline Poisson's ratio	0.4
σ_y (MPa)	Crystalline yield strength	20
h_1 (MPa)	Crystalline plastic hardening	5
h_2 (MPa)	Crystalline plastic hardening	4
q_1	Crystalline plastic hardening	2.5
q_2	Crystalline plastic hardening	3
m	Weibull shape parameter	2
s	Weibull scale parameter	1.3
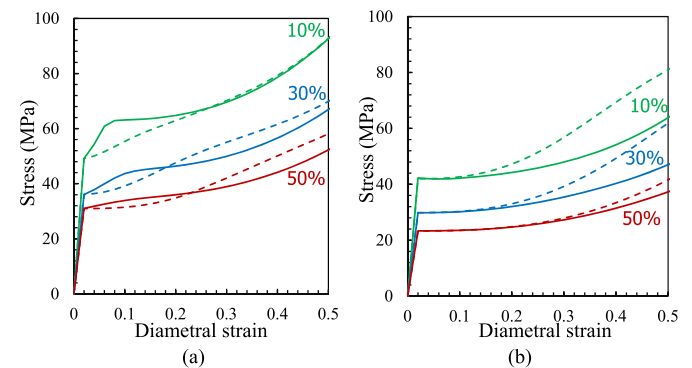
Fig. 6. Simulated stress-strain behavior for different amorphous fractions φ_0^{am} (solid lines: $s = 3$, dashed lines: $s = 1.3$) for (a) R2 and (b) R4 specimens.
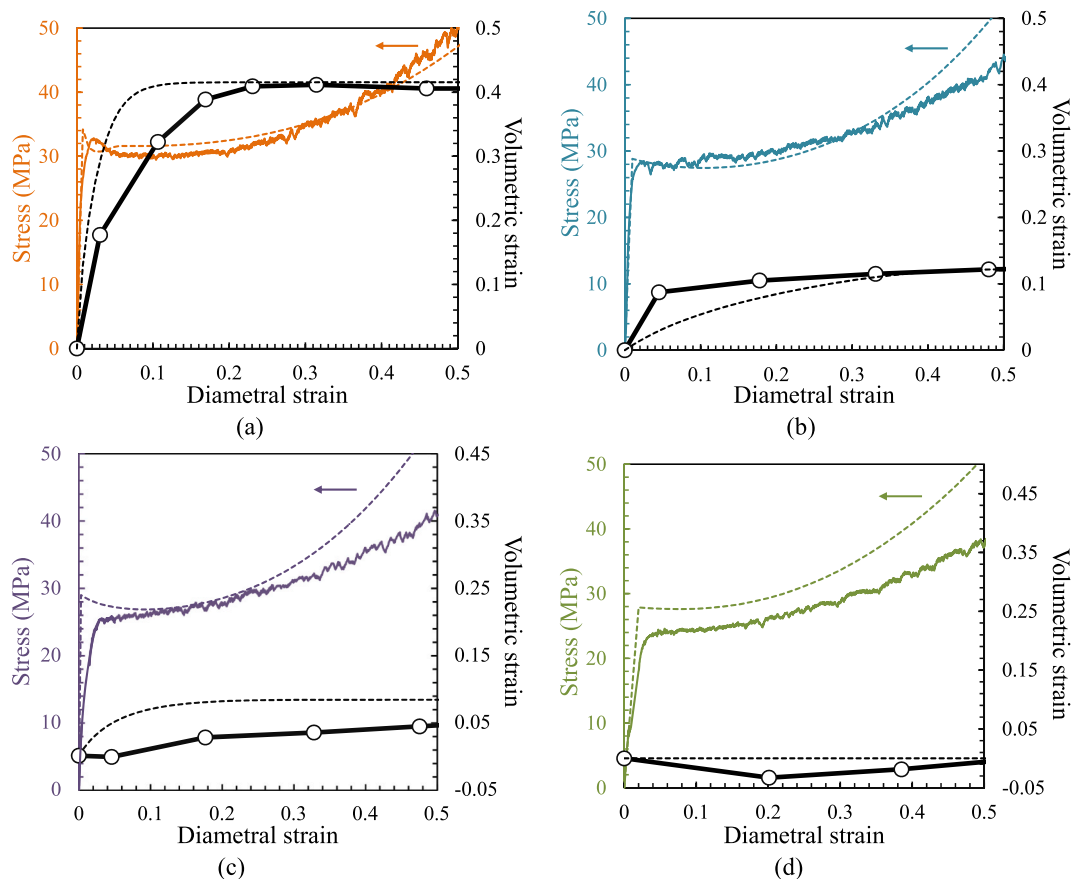
Fig. 7. Model simulations (dashed lines) vs. experiments (solid lines) of the stress-strain and volumetric behavior for (a) R2, (b) R4, (c) R10 and (d) R80 specimens.

where φ^{cry} is the crystal volume fraction, $\varphi_w^{cry} = 0.74$ is the crystal weight fraction, $\rho = 0.96$ g/cm^3 is the density of the whole material and $\rho_{cry} = 1.00$ g/cm^3 is the density of the crystalline phase. The shape factor α (see Appendix A) is taken from a previous work [20] in which the value has been extracted from the calibration of the yield surface (12) using the initial biaxial yield strength for different biaxial stress states. The crystalline elastic constants, E_{cry} and ν_{cry}, are those proposed by Choy and Leung [57]. The plastic properties of the crystalline phase, σ_y, h_1, h_2, q_1 and q_2, and the Weibull parameters, m and s, were fitted to the macro-response of the R2 specimen.

The simulation consists in a macroscopic transversal straining up to an assigned maximum value. To gain insight into the model specificities, Fig. 6 presents a parametric analysis in which a model parameter is varied independently while the others are kept constant. Here, we focus on the two lowest specimen curvature radii. A global view at these plots allows to provide indications on the effects of model parameters, related to initial microstructure and damage micromechanism, and how stress triaxiality affects their effects on the macro-response. The increase in amorphous fraction leads to a reduction of yield strength level and favors the volumetric strain increase. By controlling the volumetric strain evolution, the Weibull scale parameter has a great effect on the macro-stress that starts with a unique curve and then diverges beyond some critical diametral strain that depends on the triaxial stress state.

Fig. 7 shows the model-experiments comparison. In the simulations, the variations in specimen diameter $\dot{D} = D\dot{\bar{\varepsilon}}_D$ and curvature radius R_c are considered for every applied stress ratio R. The R2 specimen data were used to fit the plastic and damage parameters while the predictions under the other stress ratios are plotted with the experimental data to verify the model predictability. Note that the aim is not to perfectly

match the model with the experimental data but to capture the general trends of the triaxiality effect on the plastic-damage coupling. Both elastic-plastic stress-strain response and inelastic volumetric strain are satisfactory reproduced by the model, especially considering that only the R2 specimen data were used for the model identification.

4. Concluding remarks

The plastic deformation behavior of high-density polyethylene was experimentally examined under different triaxial stress states. The macroscopic stress and volumetric strain were quantified while the rate of transversal strain was controlled. The progressive cavitation damage, favored by high values of the stress triaxiality ratio, was introduced into an elastic-plastic micromechanical framework from probabilistic considerations in the form of a Weibull statistical density function. The theoretical predictions and the experimental results were found in good agreement highlighting the relevance of the constitutive representation for high-density polyethylene.

To improve correlation between theory and experiment, further investigations are needed to incorporate into the constitutive representation the elementary mechanisms operating in the crystalline lamellae.

CRediT authorship contribution statement

Amar Mesbah: Investigation, Software, Visualization, Formal analysis. **Mohamed Elmeguenni:** Investigation, Formal analysis. **Zhu Yan:** Investigation, Formal analysis. **Fahmi Zaïri:** Conceptualization, Writing – review & editing, Project administration. **Ning Ding:** Conceptualization, Writing – review & editing, Project administration. **Jean-Michel Gloaguen:** Data curation.

Declaration of competing interest

The authors declare that they have no known competing financial interests or personal relationships that could have appeared to influence the work reported in this paper.

Appendix A

$$
\begin{aligned}
\overline{T}_1 &= (3P_1 + 2P_2)^2 T_1 + 2P_1(3P_1 + 4P_2)T_2 \\
\overline{T}_2 &= 4P_2^2 T_2
\end{aligned}
\tag{A1}
$$

with

$$
T_1 = \frac{1}{15}\left(T_{11}^{(1)} + 4T_{12}^{(1)} + 4T_{21}^{(1)} + 6T_{22}^{(1)} + 2T_{11}^{(2)} - 4T_{12}^{(2)} + 2T_{22}^{(2)}\right)
$$

$$
T_2 = \frac{1}{15}\left(T_{11}^{(1)} - T_{12}^{(1)} - T_{21}^{(1)} + T_{22}^{(1)} + 2T_{11}^{(2)} + 6T_{12}^{(2)} + 7T_{22}^{(2)}\right)
\tag{A2}
$$

$$
\begin{aligned}
T_{IK}^{(1)} = &-\frac{1}{3} + \frac{\varphi^{am}}{9450(1 - \nu_{cry})^2 \left(Z_2 + S_{II}^{(2)}\right)\left(Z_2 + S_{KK}^{(2)}\right)}\left[1575\left(1 - 2\nu_{cry}\right)^2 \Gamma_{II}\Gamma_{KK}\right. \\
&+ 21\left(25\nu_{cry} - 23\right)\left(1 - 2\nu_{cry}\right)(\Gamma_{II}\Delta_K + \Gamma_{KK}\Delta_I) + 21\left(25\nu_{cry} - 2\right) \\
&\left(1 - 2\nu_{cry}\right)(\Gamma_{II} + \Gamma_{KK}) + 3\left(35\nu_{cry}^2 - 70\nu_{cry} + 36\right)\Delta_{IK} \\
&\left. + 7\left(50\nu_{cry}^2 - 59\nu_{cry} + 8\right)(\Delta_I + \Delta_K) - 2\left(175\nu_{cry}^2 - 343\nu_{cry} + 103\right)\right]
\end{aligned}
\tag{A3}
$$

$$
\begin{aligned}
T_{IJ}^{(2)} = &\frac{1}{2} + \frac{\varphi^{am}}{6300(1 - \nu_{cry})^2 \left(Z_2 + S_{IJ}^{(2)}\right)\left(Z_2 + S_{IJ}^{(2)}\right)}\left[\left(70\nu_{cry}^2 - 140\nu_{cry} - 72\right)\Delta_{IJ}\right. \\
&\left. - \left(175\nu_{cry}^2 - 266\nu_{cry} + 75\right)\frac{\Delta_I + \Delta_J}{2} + 350\nu_{cry}^2 - 476\nu_{cry} + 164\right]
\end{aligned}
$$

$$
\Delta_1 = \frac{3\left(1 - \alpha^4 f(\alpha^2)\right)}{1 - \alpha^4},
$$

$$
\Delta_2 = \Delta_3 = \frac{1}{2}(3 - \Delta_1),
$$

$$
\Delta_{11} = \frac{5\left(2 + \alpha^4 - 3\alpha^4 f(\alpha^2)\right)}{2(1 - \alpha^4)^2},
\tag{A4}
$$

$$
\Delta_{12} = \Delta_{21} = \Delta_{13} = \Delta_{31} = \frac{15\alpha^4\left[-3 + (1 + 2\alpha^4)f(\alpha^2)\right]}{4(1 - \alpha^4)^2},
$$

$$
\Delta_{22} = \Delta_{23} = \Delta_{32} = \Delta_{33} = \frac{15\alpha^4\left[1 + 2\alpha^4 + (1 - 4\alpha^4)f(\alpha^2)\right]}{16(1 - \alpha^4)^2}
$$

$$
f(\alpha) = \begin{cases} \dfrac{\cosh^{-1}\alpha}{\alpha\sqrt{\alpha^2 - 1}} & \text{if } \alpha > 1 \\[3mm] \dfrac{\cos^{-1}\alpha}{\alpha\sqrt{1 - \alpha^2}} & \text{if } \alpha < 1 \end{cases}
\tag{A5}
$$

$$
P_1 = \frac{\varphi^{am}(\Lambda_1 - \Omega_1)}{[1 + 2\varphi^{am}(\Omega_2 - \Lambda_2)][1 + \varphi^{am}(3\Omega_1 + 2\Omega_2 - 3\Lambda_1 - 2\Lambda_2)]}
$$

$$
P_2 = \frac{1}{2 + 4\varphi^{am}(\Omega_2 - \Lambda_2)}
\tag{A6}
$$

$$
\Omega_1 = \frac{1 - \Gamma_{11} - 4\Gamma_{12}}{30\left(Z_2 + S_{11}^{(2)}\right)} - \frac{1}{15\left(Z_2 + S_{12}^{(2)}\right)} + \frac{1 - 4\Gamma_{21} - 6\Gamma_{22}}{30\left(Z_2 + S_{22}^{(2)}\right)}
$$

$$
\Omega_2 = \frac{1 - \Gamma_{11} + \Gamma_{12}}{30\left(Z_2 + S_{11}^{(2)}\right)} - \frac{1}{10\left(Z_2 + S_{12}^{(2)}\right)} + \frac{7 + \Gamma_{21} - \Gamma_{22}}{60\left(Z_2 + S_{22}^{(2)}\right)}
\tag{A7}
$$

$$\Lambda_1 = \frac{\left(S_{11}^{(1)} + 4S_{21}^{(1)} + 2S_{11}^{(2)}\right)\left(1 - \Gamma_{11} - 4\Gamma_{12}\right) + 10S_{21}^{(1)}\Gamma_{12}}{30\left(Z_2 + S_{11}^{(2)}\right)} - \frac{2S_{12}^{(2)}}{15\left(Z_2 + S_{12}^{(2)}\right)}$$

$$+ \frac{\left(3S_{22}^{(1)} + 2S_{12}^{(1)} + 3S_{22}^{(2)}\right)\left(3 - 4\Gamma_{21} - 6\Gamma_{22}\right) - 6S_{22}^{(2)} + 5S_{12}^{(1)}\Gamma_{21}}{45\left(Z_2 + S_{22}^{(2)}\right)} \tag{A8}$$

$$\Lambda_2 = \frac{\left(S_{11}^{(1)} - S_{21}^{(1)} + 2S_{11}^{(2)}\right)\left(1 - \Gamma_{11} + \Gamma_{12}\right)}{30\left(Z_2 + S_{11}^{(2)}\right)} + \frac{S_{12}^{(2)}}{5\left(Z_2 + S_{12}^{(2)}\right)}$$

$$+ \frac{\left(S_{22}^{(1)} - S_{12}^{(1)} + S_{22}^{(2)}\right)\left(1 + 2\Gamma_{21} - 2\Gamma_{22}\right) + 6S_{22}^{(1)}}{30\left(Z_2 + S_{22}^{(2)}\right)}$$

$$\Gamma_{I1} = \frac{\left(Z_1 + Z_2 + S_{22}^{(1)} + S_{22}^{(2)}\right)\left(Z_1 + S_{I1}^{(1)}\right) - \left(Z_1 + S_{21}^{(1)}\right)\left(Z_1 + S_{I2}^{(1)}\right)}{\left(Z_1 + Z_2 + S_{22}^{(1)} + S_{22}^{(2)}\right)\left(Z_1 + 2Z_2 + S_{11}^{(1)} + 2S_{11}^{(2)}\right) - \left(Z_1 + S_{12}^{(1)}\right)\left(Z_1 + S_{21}^{(1)}\right)}$$

$$\tag{A9}$$

$$\Gamma_{I2} = \Gamma_{I3} = \frac{\left(Z_1 + 2Z_2 + S_{11}^{(1)} + 2S_{11}^{(2)}\right)\left(Z_1 + S_{I1}^{(1)}\right) - \left(Z_1 + S_{12}^{(1)}\right)\left(Z_1 + S_{I1}^{(1)}\right)}{2\left(Z_1 + Z_2 + S_{22}^{(1)} + S_{22}^{(2)}\right)\left(Z_1 + 2Z_2 + S_{11}^{(1)} + 2S_{11}^{(2)}\right) - 2\left(Z_1 + S_{12}^{(1)}\right)\left(Z_1 + S_{21}^{(1)}\right)}$$

$$Z_1 = \frac{\lambda_{cry}\mu_{am} - \lambda_{am}\mu_{cry}}{\left(\mu_{am} - \mu_{cry}\right)\left[2\left(\mu_{am} - \mu_{cry}\right) + 3\left(\lambda_{am} - \lambda_{cry}\right)\right]}$$

$$\tag{A10}$$

$$Z_2 = \frac{\mu_{cry}}{2\left(\mu_{am} - \mu_{cry}\right)}$$

$$\lambda_{cry} = \frac{E_{cry}\nu_{cry}}{\left(1 + \nu_{cry}\right)\left(1 - 2\nu_{cry}\right)}, \quad \mu_{cry} = \frac{E_{cry}}{2\left(1 + \nu_{cry}\right)}$$

$$\tag{A11}$$

$$\lambda_{am} = \frac{E_{am}\nu_{am}}{\left(1 + \nu_{am}\right)\left(1 - 2\nu_{am}\right)}, \quad \mu_{am} = \frac{E_{am}}{2\left(1 + \nu_{am}\right)}$$

$$S_{11}^{(1)} = \left(4\nu_{cry} + \frac{2}{\alpha^2 - 1}\right)g(\alpha) + 4\nu_{cry} + \frac{4}{3(\alpha^2 - 1)}$$

$$S_{12}^{(1)} = S_{13}^{(1)} = \left(4\nu_{cry} + \frac{2\alpha^2 + 1}{\alpha^2 - 1}\right)g(\alpha) + 4\nu_{cry} - \frac{2\alpha^2}{\alpha^2 - 1}$$

$$S_{21}^{(1)} = S_{31}^{(1)} = \left(-2\nu_{cry} - \frac{2\alpha^2 + 1}{\alpha^2 - 1}\right)g(\alpha) - \frac{2\alpha^2}{\alpha^2 - 1}$$

$$S_{22}^{(1)} = S_{23}^{(1)} = S_{32}^{(1)} = S_{33}^{(1)} = \left(-2\nu_{cry} + \frac{4\alpha^2 - 1}{4(\alpha^2 - 1)}\right)g(\alpha) + \frac{\alpha^2}{2(\alpha^2 - 1)} \tag{A12}$$

$$S_{11}^{(2)} = \left(-4\nu_{cry} + \frac{4\alpha^2 - 2}{\alpha^2 - 1}\right)g(\alpha) - 4\nu_{cry} + \frac{12\alpha^2 - 8}{3(\alpha^2 - 1)}$$

$$S_{12}^{(2)} = S_{13}^{(2)} = S_{21}^{(2)} = S_{31}^{(2)} = \left(-\nu_{cry} - \frac{\alpha^2 + 2}{\alpha^2 - 1}\right)g(\alpha) - 2\nu_{cry} - \frac{2}{\alpha^2 - 1}$$

$$S_{22}^{(2)} = S_{23}^{(2)} = S_{32}^{(2)} = S_{33}^{(2)} = \left(2\nu_{cry} - \frac{4\alpha^2 - 7}{4(\alpha^2 - 1)}\right)g(\alpha) + \frac{\alpha^2}{2(\alpha^2 - 1)}$$

$$g(\alpha) = \begin{cases} \dfrac{\alpha}{\left(\alpha^2 - 1\right)^{3/2}}\left[\cosh^{-1}\alpha - \alpha\left(\alpha^2 - 1\right)^{1/2}\right] & \text{if } \alpha > 1 \\[2em] \dfrac{\alpha}{\left(1 - \alpha^2\right)^{3/2}}\left[\alpha\left(1 - \alpha^2\right)^{1/2} - \cos^{-1}\alpha\right] & \text{if } \alpha < 1 \end{cases} \tag{A13}$$

References

[1] S. Hillmansen, S. Hobeika, R.N. Haward, P.S. Leevers, The effect of strain rate, temperature, and molecular mass on the tensile deformation of polyethylene, Polym. Eng. Sci. 40 (2000) 481–489.

[2] A.S. Argon, A. Galeski, T. Kazmierczak, Rate mechanisms of plasticity in semicrystalline polyethylene, Polymer 46 (2005) 11798–11805.

[3] T. Kazmierczak, A. Galeski, A.S. Argon, Plastic deformation of polyethylene crystals as a function of crystal thickness and compression rate, Polymer 46 (2005) 8926–8936.

[4] N.K. Bourne, J.C.F. Millett, E.N. Brown, G.T. Gray III, Effect of halogenation on the shock properties of semicrystalline thermoplastics, J. Appl. Phys. 102 (2007), 063510.

[5] E.N. Brown, R.B. Willms, G.T. Gray III, P.J. Rae, C.M. Cady, K.S. Vecchio, J. Flowers, M.Y. Martinez, Influence of molecular conformation on the constitutive response of polyethylene: a comparison of HDPE, UHMWPE, and PEX, Exp. Mech. 47 (2007) 381–393.

[6] J. Furmanski, C.P. Trujillo, D.T. Martinez, G.T. Gray III, E.N. Brown, Dynamic-tensile-extrusion for investigating large strain and high strain rate behavior of polymers, Polym. Test. 31 (2012) 1031–1037.

[7] J. Furmanski, C.M. Cady, E.N. Brown, Time-temperature equivalence and adiabatic heating at large strains in high density polyethylene and ultrahigh molecular weight polyethylene, Polymer 54 (2013) 381–390.

[8] A. Peterlin, Plastic deformation of polymers with fibrous structure, Colloid Polym. Sci. 253 (1975) 809–823.

[9] A. Peterlin, in: E. Baer (Ed.), Plastic Deformation of Crystalline Polymers in Polymeric Materials, American Society for Metals: Metals Park, Ohio, 1975, pp. 175–195.

[10] E.M. Parsons, M.C. Boyce, D.M. Parks, M. Weinberg, Three-dimensional large-strain tensile deformation of neat and calcium carbonate-filled high-density polyethylene, Polymer 46 (2005) 2257–2265.

[11] F. Addiego, A. Dahoun, C. G'Sell, J.M. Hiver, Characterization of volume strain at large deformation under uniaxial tension in high-density polyethylene, Polymer 47 (2006) 4387–4399.

[12] A. Pawlak, Cavitation during tensile deformation of high-density polyethylene, Polymer 48 (2007) 1397–1409.

[13] Z. Bartczak, A. Galeski, Plasticity of semicrystalline polymers, Macromol. Symp. 294 (2010) 67–90.

[14] F. Detrez, S. Cantournet, R. Seguela, Plasticity/damage coupling in semi-crystalline polymers prior to yielding: micromechanisms and damage law identification, Polymer 52 (2011) 1998–2008.

[15] M. Ponçot, F. Addiego, A. Dahoun, True intrinsic mechanical behaviour of semi-crystalline and amorphous polymers: influences of volume deformation and cavities shape, Int. J. Plast. 40 (2013) 126–139.

[16] Y. Zhang, P.Y. Ben Jar, S. Xue, L. Li, Quantification of strain-induced damage in semi-crystalline polymers: a review, J. Mater. Sci. 54 (2019) 62–82.

[17] M. Elmeguenni, M. Naït-Abdelaziz, F. Zaïri, J.M. Gloaguen, Fracture characterization of high-density polyethylene pipe materials using the J-integral and the essential work of fracture, Int. J. Fract. 183 (2013) 119–133.

[18] H. Zhang, Z. Zhou, A. Chudnovsky, Applying the crack-layer concept to modeling of slow crack growth in polyethylene, Int. J. Eng. Sci. 83 (2014) 42–56.

[19] G. Arora, H. Pathak, Experimental and numerical approach to study mechanical and fracture properties of high-density polyethylene carbon nanotubes composite, Materials Today Communications 22 (2020) 100829.

[20] K. Hachour, F. Zaïri, M. Naït-Abdelaziz, J.M. Gloaguen, M. Aberkane, J. M. Lefebvre, Experiments and modeling of high-crystalline polyethylene yielding under different stress states, Int. J. Plast. 54 (2014) 1–18.

[21] S. Castagnet, Y. Deburck, Relative influence of microstructure and macroscopic triaxiality on cavitation damage in a semi-crystalline polymer, Mater. Sci. Eng. A448 (2007) 56–66.

[22] L. Laiarinandrasana, J. Besson, M. Lafarge, G. Hochstetter, Temperature dependent mechanical behaviour of PVDF: experiments and numerical modelling, Int. J. Plast. 25 (2009) 1301–1324.

[23] G. Boisot, L. Laiarinandrasana, J. Besson, C. Fond, G. Hochstetter, Experimental investigations and modeling of volume change induced by void growth in polyamide 11, Int. J. Solid Struct. 48 (2011) 2642–2654.

[24] C. Zhang, I.D. Moore, Nonlinear mechanical response of high density polyethylene. Part II: uniaxial constitutive modelling, Polym. Eng. Sci. 37 (1997) 413–420.

[25] O.U. Colak, N. Dusunceli, Modeling viscoelastic and viscoplastic behavior of high density polyethylene (HDPE), J. Eng. Mater. Technol. 128 (2006) 572–578.

[26] F. Zaïri, B. Aour, J.M. Gloaguen, M. Naït-Abdelaziz, J.M. Lefebvre, Numerical modelling of elastic-viscoplastic equal channel angular extrusion process of a polymer, Comput. Mater. Sci. 38 (2006) 202–216.

[27] H. Ben Hadj Hamouda, L. Laiarinandrasana, R. Piques, Viscoplastic behaviour of a medium density polyethylene (MDPE): constitutive equations based on double nonlinear deformation model, Int. J. Plast. 23 (2007) 1307–1327.

[28] F. Bédoui, J. Diani, G. Régnier, W. Seiler, Micromechanical modelling of isotropic elastic behaviour of semicrystalline polymers, Acta Mater. 54 (2006) 1513–1523.

[29] O. Gueguen, S. Ahzi, A. Makradi, S. Belouettar, A new three-phase model to estimate the effective elastic properties of semi-crystalline polymers: application to PET, Mech. Mater. 42 (2010) 1–10.

[30] K. Anoukou, F. Zaïri, M. Naït-Abdelaziz, A. Zaoui, Z. Qu, J.M. Gloaguen, J. M. Lefebvre, A micromechanical model taking into account the contribution of α- and γ-crystalline phases in the stiffening of polyamide 6-clay nanocomposites: a closed-formulation including the crystal symmetry, Composites Part B 64 (2014) 84–96.

[31] B.J. Lee, D.M. Parks, S. Ahzi, Micromechanical modeling of large plastic deformation and texture evolution in semi-crystalline polymers, J. Mech. Phys. Solid. 41 (1993) 1651–1687.

[32] B.J. Lee, A.S. Argon, D.M. Parks, S. Ahzi, Z. Bartczak, Simulation of large strain plastic deformation and texture evolution in high density polyethylene, Polymer 34 (1993) 3555–3575.

[33] S. Nikolov, I. Doghri, A micro/macro constitutive model for the small-deformation behavior of polyethylene, Polymer 41 (2000) 1883–1891.

[34] S. Nikolov, I. Doghri, O. Pierard, L. Zealouk, A. Goldberg, Multi-scale constitutive modeling of the small deformations of semi-crystalline polymers, J. Mech. Phys. Solid. 50 (2002) 2275–2302.

[35] J.A.W. van Dommelen, D.M. Parks, M.C. Boyce, W.A.M. Brekelmans, F.P. T. Baaijens, Micromechanical modeling of the elasto-viscoplastic behavior of semi-crystalline polymers, J. Mech. Phys. Solid. 51 (2003) 519–541.

[36] M. Agoras, P. Ponte Castaneda, Multi-scale homogenization-based modeling of semi-crystalline polymers, Phil. Mag. 92 (2012) 925–958.

[37] M. Uchida, N. Tada, Micro-, meso- to macroscopic modeling of deformation behavior of semi-crystalline polymer, Int. J. Plast. 49 (2013) 164–184.

[38] M. Mirkhalaf, J.A.W. van Dommelen, L.E. Govaert, J. Furmanski, M.G.D. Geers, Micromechanical modeling of anisotropic behavior of oriented semicrystalline polymers, J. Polym. Sci. B Polym. Phys. 57 (2019) 378–391.

[39] A.D. Drozdov, J. Christiansen, Modelling the viscoplastic response of polyethylene in uniaxial loading-unloading tests, Mech. Res. Commun. 30 (2003) 431–442.

[40] N. Dusunceli, O.U. Colak, Modelling effects of degree of crystallinity on mechanical behavior of semicrystalline polymers, Int. J. Plast. 24 (2008) 1224–1242.

[41] G. Ayoub, F. Zaïri, M. Naït-Abdelaziz, J.M. Gloaguen, Modelling large deformation behaviour under loading-unloading of semicrystalline polymers: application to a high density polyethylene, Int. J. Plast. 26 (2010) 329–347.

[42] G. Ayoub, F. Zaïri, C. Fréderix, J.M. Gloaguen, M. Naït-Abdelaziz, R. Seguela, J. M. Lefebvre, Effects of crystal content on the mechanical behaviour of polyethylene under finite strains: experiments and constitutive modelling, Int. J. Plast. 27 (2011) 492–511.

[43] A.D. Drozdov, R. Klitkou, J.D. Christiansen, Multi-cycle deformation of semicrystalline polymers: observations and constitutive modeling, Mech. Res. Commun. 48 (2013) 70–75.

[44] H. Abdul-Hameed, T. Messager, F. Zaïri, M. Naït-Abdelaziz, Large-strain viscoelastic-viscoplastic constitutive modeling of semi-crystalline polymers and model identification by deterministic/evolutionary approach, Comput. Mater. Sci. 90 (2014) 241–252.

[45] M. Makki, G. Ayoub, H. Abdul-Hameed, F. Zaïri, B. Mansoor, M. Naït-Abdelaziz, M. Ouederni, F. Zaïri, Mullins effect in polyethylene and its dependency on crystal content: a network alteration model, J. Mech. Beh. Biomed. Mater. 75 (2017) 442–454.

[46] H. Sepiani, M.A. Polak, A. Penlidis, Modeling short- and long-term time-dependent nonlinear behavior of polyethylene, Mech. Adv. Mater. Struct. 25 (2018) 600–610.

[47] K. Chen, G. Kang, C. Yu, H. Jiang, Effect of crystalline content on ratchetting of ultra-high molecular weight polyethylene polymers: experimental investigation and constitutive model, Mech. Mater. 133 (2019) 37–54.

[48] T. Deplancke, M. Fivel, O. Lame, 1D strain rate-dependent constitutive model of UHMWPE: from crystalline network to fibrillar structure behavior, Mech. Mater. 137 (2019) 103129.

[49] Z. Qi, N. Hu, G. Li, D. Zeng, Constitutive modeling for the elastic-viscoplastic behavior of high density polyethylene under cyclic loading, Int. J. Plast. 113 (2019) 125–144.

[50] C.A. Bernard, O. Lame, T. Deplancke, J.Y. Cavaillé, K. Ogawa, From rheological to original three-dimensional mechanical modelling of semi-crystalline polymers: application to a wide strain rate range and large deformation of Ultra-High Molecular Weight PolyEthylene, Mech. Mater. 151 (2020) 103640.

[51] B. Wunderlich, in: Macromolecular Physics, Crystal Melting, vol. 3, Academic Press, New York, 1980.

[52] P.W. Bridgman, The stress distribution at the neck of a tension specimen, Transactions ASME 32 (1944) 553–574.

[53] D. Heikens, S.D. Sjoerdsma, W.J. Coumans, A mathematical relation between volume strain, elongational strain and stress in homogeneous deformation, J. Mater. Sci. 16 (1981) 429–432.

[54] F. Zaïri, M. Naït-Abdelaziz, K. Woznica, J.M. Gloaguen, Constitutive equations for the viscoplastic-damage behaviour of a rubber-modified polymer, Eur. J. Mech. Solid. 24 (2005) 169–182.

[55] J.W. Ju, L.Z. Sun, Effective elastoplastic behavior of metal matrix composites containing randomly located aligned spheroidal inhomogeneities. Part I: micromechanics-based formulation, Int. J. Solid Struct. 38 (2001) 183–201.

[56] H.T. Liu, L.Z. Sun, Multi-scale modeling of elastoplastic deformation and strengthening mechanisms in aluminium-based amorphous nanocomposites, Acta Mater. 53 (2005) 2693–2701.

[57] C.L. Choy, W.P. Leung, Elastic moduli of ultradrawn polyethylene, J. Polym. Sci. B Polym. Phys. 23 (1985) 1759–1780.